High Thermal Robustness of Molecularly Thin Perovskite Nanosheets and Implications for Superior Dielectric Properties

Bao-Wen Li,[†] Minoru Osada,[†,‡,*] Yasuo Ebina,[†,‡] Kosho Akatsuka,[†,‡] Katsutoshi Fukuda,[†,‡] and Takayoshi Sasaki[†,‡,*]

[†]International Center for Materials Nanoarchitectonics (MANA), National Institute for Materials Science, Tsukuba, Ibaraki 305-0044, Japan and [‡]CREST, Japan Science and Technology Agency, Kawaguchi, Saitama 332-0012, Japan

ABSTRACT A systematic study has been conducted to examine the thermal stability of layer-by-layer assembled films of perovskite-type nanosheets, $(Ca_2Nb_3O_{10}^-)_n$ (n = 1−10), which exhibit superior dielectric and insulating properties. In-plane and out-of-plane X-ray diffraction data as well as observations by atomic force microscopy and transmission electron microscopy indicated the high thermal robustness of the nanosheet films. In a monolayer film with an extremely small thickness of ~2 nm, the nanosheet was stable up to 800 °C, the temperature above which segregation into $CaNb_2O_6$ and $Ca_2Nb_2O_7$ began. The critical temperature moderately decreased as the film thickness, or the number of nanosheet layers, increased, and reached 700 °C for seven- and 10-layer films, which is comparable to the phase transformation temperature for a bulk phase of the protonic layered oxide of $HCa_2Nb_3O_{10}\cdot 1.5H_2O$ as a precursor of the nanosheet. This thermal stabilization of perovskite-type nanosheets should be associated with restricted nucleation and crystal growth peculiar to such ultrathin 2D bound systems. The stable high-k dielectric response (ε_r = 210) and highly insulating nature ($J < 10^{-7}$ A cm^{-2}) remained substantially unchanged even after the nanosheet film was annealed up to 600 °C. This study demonstrates the high thermal stability of 2D perovskite-type niobate nanosheets in terms of structure and dielectric properties, which suggests promising potential for future high-k devices operable over a wide temperature range.

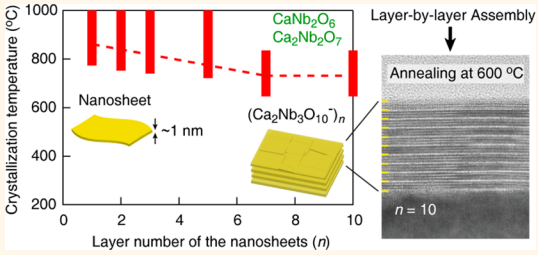

KEYWORDS: perovskite-type nanosheets · layer-by-layer assembly · thermal stability · nanodielectrics

The challenge of integrating complex perovskite oxides into multilayers and heterostructures with interesting functional properties such as dielectric, magnetic, and superconducting properties has stimulated the development of layer-by-layer epitaxial thin-film growth.[1] Underlying these studies is the technical prerequisite of thin-film growth with a single-unit-cell control and an atomically sharp interface. This prerequisite has usually been achieved *via* pulsed laser deposition or molecular-beam epitaxy. In layered perovskite oxides, however, crystal growth behavior is not yet well enough established because of the particular features related to their complex and often anisotropic structures with a relatively large number of constituent elements. Understanding the growth process and consequently being able to control the interface morphology and microstructure are of fundamental interest and importance for the fabrication of devices composed of these materials.

Such a challenge is clearly exposed in perovskite-based dielectric/ferroelectric thin films with few nanometer thicknesses. Continuing demands to further miniaturize electronic devices create problems concerning the size effects of dielectricity and ferroelectricity.[2] Perovskite thin films often yield reduced permittivity and polarization values that are 1 order of magnitude smaller than bulk values,[3−11] although experimental results have demonstrated that dielectricity/ferroelectricity persist down to a film thickness of a few unit cells.[12−15] In this context, knowledge concerning the crystallization behavior of two-dimensional (2D) perovskite

* Address correspondence to osada.minoru@nims.go.jp; sasaki.takayoshi@nims.go.jp.

Received for review July 31, 2013 and accepted May 5, 2014.

Published online May 05, 2014
10.1021/nn502014c

layers with thicknesses of a few octahedra becomes increasingly important due to the integration of perovskite-type nanofilms into nanoelectronics as well as fundamental concerns about the size effects.

Recent advances in 2D oxide nanosheets offer a new opportunity for the layer-by-layer fabrication of oxide thin films.[16,17] Oxide nanosheets obtained *via* the exfoliation of layered compounds possess a high 2D anisotropy with a molecular thickness (typically 1−2 nm) and, therefore, can be regarded as the thinnest self-standing 2D nanostructures retaining functionalities inherent from the parent compounds.[16−18] In addition, due to their polyelectrolytic nature, these structures can be employed as building blocks for electrostatic layer-by-layer self-assembly.[19,20] Research on such 2D systems has recently intensified because of the successful exfoliation of transition-metal oxides including $Ti_{1-\delta}O_2^{4\delta-}$,[21,22] $MnO_2^{\delta-}$,[23,24] and perovskite oxides.[25] In the perovskite case, the exfoliation of layered perovskites has been reported for Dion−Jacobson phases including $LaNb_2O_7^-$, $(Ca,Sr)_2(Nb,Ta)_3O_{10}^-$, $Ca_2Na_{m-3}Nb_mO_{3m+1}^-$ (m = 4−6), $CaLaNb_2TiO_{10}^-$, and $La_2Ti_2NbO_{10}^-$ and others with Ruddlesden−Popper ($Eu_{0.56}Ta_2O_7^{2-}$, $SrLaTi_2TaO_{10}^{2-}$, $Ca_2Ta_2TiO_{10}^{2-}$) and Aurivillius ($Sr_{0.85}Bi_{0.21}Ta_2O_7^{2-}$, $Bi_4Ti_3O_{12}^{2-}$) phases.[25−31] We recently reported that multilayer films of $Ca_2Nb_3O_{10}^-$ and $Sr_2Nb_3O_{10}^-$ nanosheets exhibited high permittivity constants (ε_r = 210−240) and low leakage current densities (<10^{-7} A/cm^2) even at a few-nanometer thickness.[32,33] This performance is far superior to that of other high-k materials extensively studied thus far including (Ba, Sr)TiO_3 in typical perovskite structure (not in 2D nanosheet form). Thus, these nanosheets can be considered as promising candidates, fulfilling an essential requirement for next-generation high-k devices such as capacitors and gate dielectrics.[25]

To guide practical uses of this emerging class of materials, there is a critical need for understanding the thermal stability in structural and dielectric properties. This issue is of importance both for future applications in high-temperature devices and for device integrations in current fabrication lines. In recent years, there is a strong demand for the development of high-temperature capacitors. Capacitors are ubiquitous in electronic devices and systems; automotive and many other industries have applications that share the same key requirements of reliability under harsh operating condition at >200 °C. In addition, current device fabrications often require high-temperature annealing (>500 °C), causing degradation problems arising from interface reactions and thermal strain with underlying substrates. Accurate knowledge concerning the thermal behavior and its impact on dielectric performance in perovskite nanosheets is highly required.

Perovskite-type nanosheets are also an interesting playground for crystal chemistry in 2D materials. In molecularly thin 2D perovskite layers, nucleation and crystal growth may be severely hindered, and such a 2D bound reactant provides an unusual environment in structure reconstruction, causing new forms of dielectric/ferroelectric states. An important aspect is that these nanosheets consist of molecularly thin perovskite layers with a controlled octahedron thickness. This feature makes perovskite-type nanosheets an ideal base for an investigation on the control of crystallization with a critical thickness. In this context, we previously observed unusual crystallization behaviors of anatase nanocrystallites from nanofilms composed of $Ti_{0.87}O_2^{0.52-}$ nanosheets.[34] The crystallization of anatase from $Ti_{0.87}O_2^{0.52-}$ nanosheets was suppressed up to 800 °C in its monolayer film, approximately 400 °C higher than a normal crystallization temperature from bulk reactants. These observations provide new insights into nucleation and crystal growth in functional oxide films from a 2D atomic-layer viewpoint. However, such possibilities in perovskites have hardly been explored to date.

Here we selected perovskite-type nanosheets of $Ca_2Nb_3O_{10}^-$ with three NbO_6-octahedra thickness. In this study, we performed a systematic investigation of the thermal behavior of the high-quality monolayer and multilayer films of $(Ca_2Nb_3O_{10}^-)_n$ (n = 1−10) using in-plane and out-of-plane X-ray diffraction (XRD), atomic force microscopy (AFM), and transmission electron microscopy (TEM). We observed robust thermal stability (>700 °C) of the layered structure in such perovskite-type films with a thickness of <10 nm (n < 7); above the critical temperature, a dehydrated product of "$Ca_2Nb_3O_{9.5}$" was decomposed into a mixture of $CaNb_2O_6$ and $Ca_2Nb_2O_7$. The transformation temperature moderately decreased with the film thickness, and bulk behavior appeared for films thicker than ∼10 nm.

RESULTS AND DISCUSSION

Fabrication of Mono- and Multilayer Films of Perovskite-Type Nanosheets. The perovskite-type $Ca_2Nb_3O_{10}^-$ nanosheet was prepared by delaminating a layered perovskite of $KCa_2Nb_3O_{10}$ with a tetrabutylammonium (TBA) hydroxide solution according to a previously described procedure.[27] The resulting colloidal suspension contained monodispersed nanosheets with a unique thickness of 2.3 nm and a lateral size of 2−5 μm. We utilized the Langmuir−Blodgett (LB) technique for layer-by-layer assembly of the nanosheet as a building block. Under optimized conditions, the highly organized monolayer films were successfully prepared onto various substrates, such as quartz glass, $SrRuO_3$, and Si wafer (Supporting Information, Figure S1). AFM observation revealed that the obtained monolayer films were uniform over a large area (100 × 100 μm^2) with a surface coverage of ∼95% and negligible nanosheet overlap. An atomically flat surface was attained with an RMS (root-mean-square roughness) value of ∼0.5 nm.

Repeating the LB transfer procedure yielded multilayer films of the nanosheet, which was confirmed by

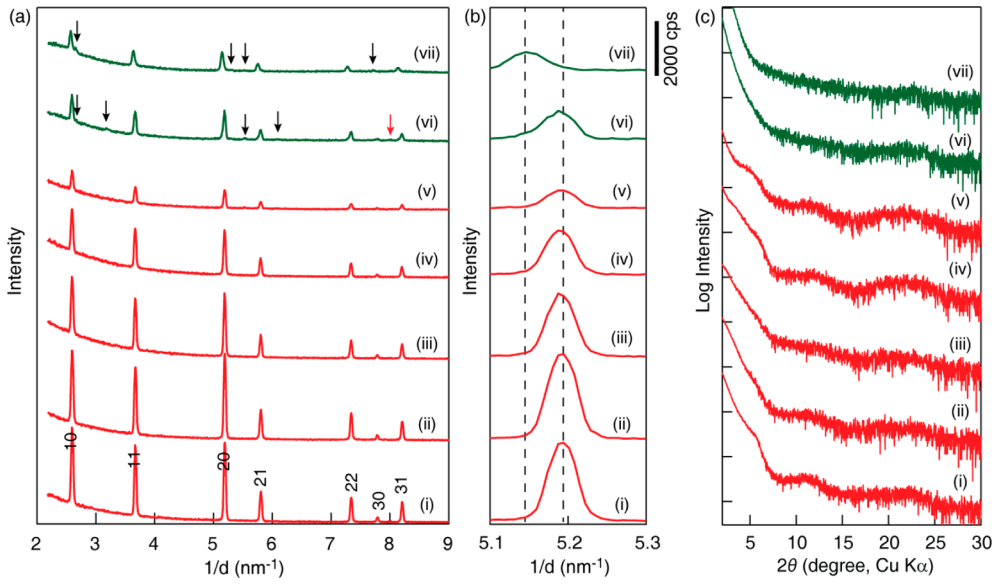

Figure 1. (a, b) In-plane and (c) out-of-plane XRD patterns for the monolayer films heated at (i) 300, (ii) 400, (iii) 500, (iv) 600, (v) 700, (vi) 800, and (vii) 900 °C. Panel (b) shows the magnified profile of (a) around 5.2 nm^{-1}. The black and red arrows indicate peaks from $CaNb_2O_6$ and $Ca_2Nb_2O_7$, respectively.

the progressive enhancement of the ultraviolet (UV) absorption band due to the nanosheet.[35,36,20] The AFM images suggested that a highly organized film texture was maintained, although it became more difficult to resolve the nanosheets with an increasing number of deposition cycles due to a gradual increase in surface roughness. The as-deposited films accommodated TBA^+ ions as a delaminating agent or their decomposed product in the nanosheet gallery. After the completion of multilayer buildup, the films were exposed to UV light for a prolonged time, and the final product was identified as an inorganic multilayer assembly accommodating $H^+(H_3O^+)$ or NH_4^+ ions due to the total photocatalytic decomposition of TBA^+ ions. The resultant film exhibited 00*l* basal reflections attributable to the multilayer structure. The films with a substantial number of nanosheet layers, e.g., 10-layer films, exhibited sharp peaks up to the eighth-order line, indicating high structural order. The gallery height of 1.55 nm in the films was similar to that (d = 1.61 nm) for the bulk protonic compound of $HCa_2Nb_3O_{10}\cdot 1.5H_2O$. These data support the construction of high-quality multilayer films, which is suitable for the present study.

Thermal Behavior of Films of Perovskite-Type Nanosheets. The nanosheet films of $(Ca_2Nb_3O_{10}^-)_n$ with various layer numbers (n = 1, 2, 3, 5, 7, 10) on a Si wafer were heated in air for 1 h at temperatures ranging from 100 to 1000 °C, and the resulting samples were examined by in-plane and out-of-plane XRD, AFM, and cross-sectional TEM. Figure 1 presents in-plane and out-of-plane XRD patterns in the heating process up to 900 °C for the monolayer film of $Ca_2Nb_3O_{10}^-$ nanosheets. The as-deposited film exhibited seven sharp diffraction peaks at 2.59, 3.67, 5.19, 5.81, 7.34, 7.79, and 8.21 nm^{-1}, which are indexable to 10, 11, 20, 21, 22, 30, and 31, respectively, for a 2D square unit cell (a = 0.3851(2) nm) of the perovskite-type $Ca_2Nb_3O_{10}^-$ nanosheet. However, the out-of-plane data did not reveal a well-defined pattern but a very faint, broad, and wavy feature, which is due to the monolayer nature of the sample. In the heating process, there was a negligible change up to 800 °C; however, a clear shift of the in-plane XRD peaks was observed above 800 °C. For example, the strongest 20 peak from the nanosheet exhibited an apparent shift at 800 °C, and new weak peaks indicated by arrows were detected for the samples heated at 800 and 900 °C, suggesting some structural change.

The data for two-layer and three-layer films are depicted in Figures 2 and 3, respectively. The in-plane data exhibited sharp diffraction peaks, which are identical to those observed in the monolayer film. The 20 peak position remained constant at $1/d$ = 5.2 nm^{-1} up to a temperature of 700 °C and then shifted to a smaller $1/d$ value, and additional peaks appeared, which is similar to the case of the monolayer film. However, the temperature for these events was lower than that for the monolayer film. Focusing on the data at 800 °C, the peak shift became progressively larger from the monolayer to the two-layer and then the three-layer film. In contrast to the monolayer film, the two- and three-layer films exhibited a series of out-of-plane XRD peaks, which arise from the lamellar structure of the stacked nanosheets having a separation of 1.55 nm as mentioned above. The peak profile for the two-layer film was very broad due to the pairwise structure as the minimum number to induce X-ray interference, while that of the three-layer sample was better-defined and stronger. The multilayer structure appeared to be stable up to 700 °C except for an

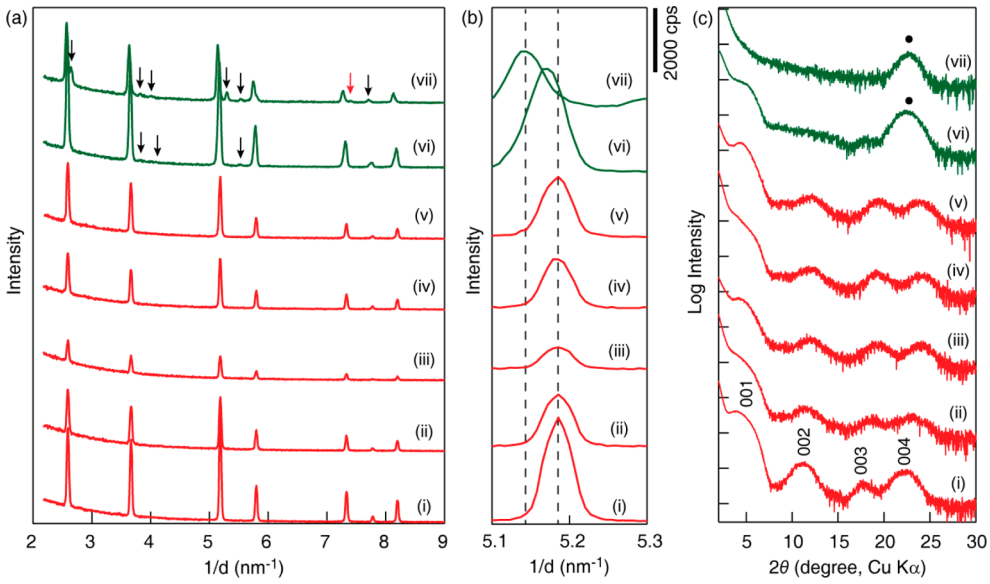

Figure 2. (a, b) In-plane and (c) out-of-plane XRD patterns for the two-layer films heated at (i) 300, (ii) 400, (iii) 500, (iv) 600, (v) 700, (vi) 800, and (vii) 900 °C. Panel (b) shows the magnified profile of (a) around 5.2 nm^{-1}. The black and red arrows indicate peaks from $CaNb_2O_6$ and $Ca_2Nb_2O_7$, respectively. The dots in (c) denote the 400 peak from $CaNb_2O_6$.

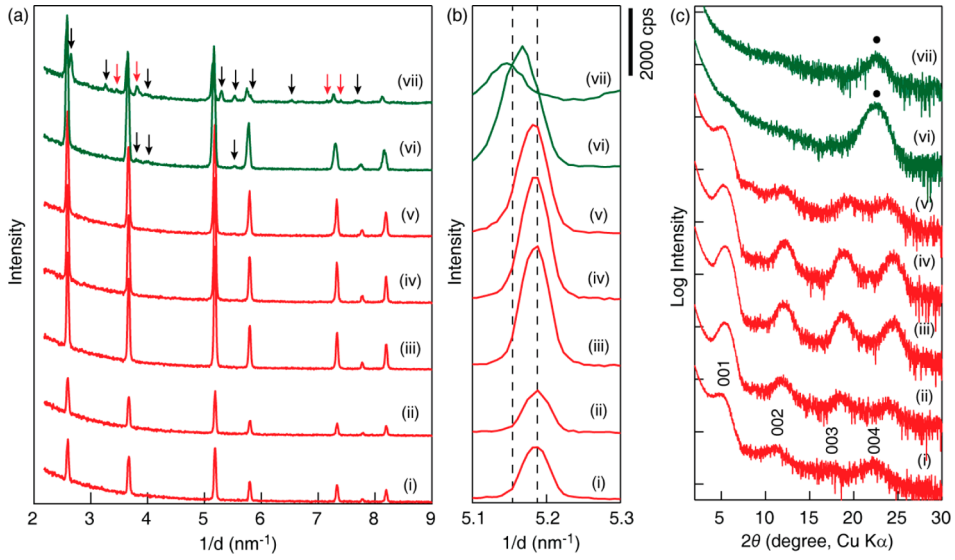

Figure 3. (a, b) In-plane and (c) out-of-plane XRD patterns for the three-layer films heated at (i) 300, (ii) 400, (iii) 500, (iv) 600, (v) 700, (vi) 800, and (vii) 900 °C. Panel (b) shows the magnified profile of (a) around 5.2 nm^{-1}. The black and red arrows indicate peaks from $CaNb_2O_6$ and $Ca_2Nb_2O_7$, respectively. The dots in (c) denote the 400 peak from $CaNb_2O_6$.

intersheet shrinkage to 1.45 nm at 400 °C (Supporting Information, Figure S5). However, the pattern exhibited a drastic change above 700 °C into one with a strong peak at 2θ = 22.5°, suggesting the collapse of the multilayer structure of stacked nanosheets. This change should be associated with changes in the in-plane data, particularly the appearance of tiny peaks. One noteworthy point is that the multilayer structure persisted at 800 °C in the two-layer film while completely disappearing in the three-layer one.

The films with larger layer numbers, n = 5, 7, 10, exhibited similar features as depicted in Supporting Information (Figures S2 to S4). The sharp in-plane peaks assignable to the perovskite-type 2D lattice were unchanged up to a critical temperature of ~700 °C, above which reflections due to the nanosheet underwent a shift and small peaks evolved. The out-of-plane patterns exhibited a well-defined basal diffraction series attributable to the multilayer structure of the stacked nanosheets, which also transformed into a completely different pattern at the critical temperature. The temperature at which these changes occurred had a tendency to gradually decrease as the number of nanosheet layers increased.

Interpretation of Structural Change. The sharp in-plane XRD data appeared to remain virtually unchanged up to the critical temperature of 700−800 °C, which is

dependent on the number of the nanosheet layers. This finding indicates that the nanosheet structure was intact below the critical temperature. The out-of-plane data also seemingly support this result, showing the stability of the lamellar structure up to such temperatures. However, the intactness of the nanosheet structure up to 600 °C is not likely from a chemical viewpoint. The as-deposited films are composed of stacked $Ca_2Nb_3O_{10}^-$ nanosheets accommodating counterions such as H^+ and NH_4^+. Such a system should not be stable above 300−400 °C, where cationic species will evaporate. Thus, we expect a chemical change as follows:

$$(H^+/NH_4^+)Ca_2Nb_3O_{10}^- \rightarrow H^+Ca_2Nb_3O_{10}^- \rightarrow Ca_2Nb_3O_{9.5} + 0.5H_2O \quad (1)$$

The volatile components leave as H_2O, depriving lattice oxygen. The small shrinkage of the intersheet separation at 400 °C from 1.55 to 1.45 nm (Supporting Information, Figure S5) may be associated with this transformation. It is reasonable to assume that the resulting $Ca_2Nb_3O_{9.5}$ with oxygen vacancies can maintain a perovskite-type framework, resulting in a negligible change in the XRD data. This result may be due to the high stability of the perovskite structure and a relatively small amount of defects being introduced.

The heating behavior of the powder sample of the protonic layered perovskite of $HCa_2Nb_3O_{10}\cdot 1.5H_2O$, the precursor of the nanosheet in this study, provides valuable information in identifying the evolved phases observed in the film samples (Supporting Information, Figure S6a). In a previous work by Fang and Mallouk,[37] the formation of a metastable form of $Ca_4Nb_6O_{19}$, with the same stoichiometry of $Ca_2Nb_3O_{9.5}$ above, was proposed for a product upon completion of dehydration at 200−300 °C. These authors discussed the phase in terms of a hypothetical structure resulting from the condensation of half of the perovskite-type slabs.[37] This structure may at least partially account for the product in this study. However, we speculate that the formation of a neutral perovskite slab of $Ca_2Nb_3O_{9.5}$ is more likely. In these films, the perovskite-type nanosheets are stacked in a disordered fashion without regular intersheet registry, involving random lateral shifts and rotation with each other, which makes it difficult for topotactic condensation to occur. To confirm this hypothesis, we synthesized a flocculated sample by restacking the nanosheets with a HCl solution, which also have a turbostratic stacking similar to the films. The sample heated at 300 °C and above exhibited a broad XRD pattern (Supporting Information, Figure S6b), which is similar to that for $Ca_2Nb_3O_{9.5}$ from the films and also to that for $Ca_4Nb_6O_{19}$ from the polycrystalline protonated sample of $HCa_2Nb_3O_{10}\cdot 1.5H_2O$. It is to be noted that the basal spacing for the flocculated sample and the films was somewhat larger than that for the polycrystalline sample. The larger spacing may suggest the formation of $Ca_2Nb_3O_{9.5}$ without condensation between neighboring perovskite-type slabs.

A comparison of the data in the heating process between the film samples of the nanosheet and the powder sample of $HCa_2Nb_3O_{10}\cdot 1.5H_2O$ is also very helpful in gaining an understanding of the changes above the critical temperature of 700−800 °C. The powder sample underwent segregation into $CaNb_2O_6$ and $Ca_2Nb_2O_7$ from "$Ca_4Nb_6O_{19}$" at 800 °C and above (Supporting Information, Figure S6), which is consistent with the previous report.[37] The data from the nanosheet films suffered from low intensity due to their scant quantities. To ensure reliable identification, we start from the data for samples heated at 1000 °C, which produced patterns with the highest signal-to-noise ratio (see Figure 4). The diffraction peaks for the 10-layer film, both in-plane and out-of-plane data, are clearly attributable to those from $CaNb_2O_6$ and $Ca_2Nb_2O_7$ in terms of the following segregation process.

$$Ca_2Nb_3O_{9.5} \rightarrow CaNb_2O_6 + 1/2Ca_2Nb_2O_7 \quad (2)$$

The data can be reasonably understood in terms of the mixture of the above two phases. Almost all the peaks could be indexed based on an orthorhombic structure

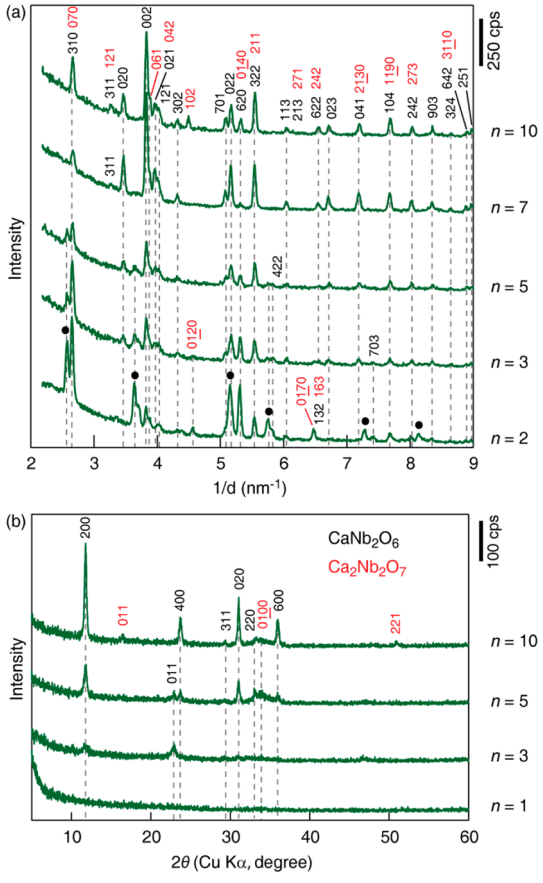

Figure 4. (a) In-plane and (b) out-of-plane XRD patterns for mono- and multilayer films heated at 1000 °C. The indices in black and red are for $CaNb_2O_6$ and $Ca_2Nb_2O_7$, respectively. The dots denote reflections from nanosheets.

for either $CaNb_2O_6$ (a = 1.4873 nm, b = 0.5775 nm, c = 0.5224 nm) or $Ca_2Nb_2O_7$ (a = 0.3831 nm, b = 2.6303 nm, c = 0.5471 nm), although some peaks overlapped and are attributed to both phases. The obtained unit cell parameters agree well with those reported previously.[38,39] The strong peak at ~23.7° in 2θ (and a smaller one at ~11.8°) observed in the out-of-plane data after the loss of the basal series peaks can be ascribed to 400 (and 200) peaks from $CaNb_2O_6$.

Next, we focus on the thermal change in the temperature range 700−900 °C based on the above interpretation from the data at 1000 °C. The in-plane XRD data in this region clearly revealed the presence of the nanosheet along with $CaNb_2O_6$ and $Ca_2Nb_2O_7$. The small peaks indicated by arrows in Figures 1−3 and S2−S4 can be assigned to those from these two phases. The fraction of $CaNb_2O_6$ and $Ca_2Nb_2O_7$ increased as the temperature increased. Thus, this process can be regarded as a transient stage where the nanosheet underwent segregation into a mixture of $CaNb_2O_6$ and $Ca_2Nb_2O_7$. As mentioned above, the peaks from the nanosheet exhibited a shift toward a lower angle side, indicating a 2D lattice expansion of approximately 1% (Supporting Information, Figure S5). This slight lattice expansion may be associated with decomposition.

Importantly, the temperature range where these events occurred depends on the film thickness or the number of nanosheet layers. The monolayer film exhibited a very slight shift of the 20 peak from the nanosheet at 800 °C, which became pronounced at 900 °C. By increasing the number of nanosheet layers, the temperature for the peak shift decreased. In addition, the abundance of the decomposed products of $CaNb_2O_6/Ca_2Nb_2O_7$ was more significant at the same temperature for the thicker film samples. Even the seven- and 10-layer films began to show a clear change at 700 °C. Furthermore, the abundance of the persisting nanosheet decreased as the number of nanosheet layers in the films increased when compared with samples heated at the same temperature. The decomposition was complete at 1000 °C for the samples of more than five layers, while the nanosheet survived in the thinner films at this temperature.

Figure 5 plots the temperature range where these events, such as decomposition and nanosheet expansion, occurred. The temperature range for these changes is dependent on the film thickness. The nanosheet could survive at higher temperatures in the thinner films. The decomposition temperature range gradually decreases by ~100 °C between the monolayer and 10-layer sample. The decomposition temperature of the 10-layer film may be regarded as comparable to that of the bulk powder sample from comparison with the behavior of the powder sample. This unique thermal behavior should be closely associated with the abundance of the nanosheet of $Ca_2Nb_3O_{10}^-$ as a "reactant" and its configuration.

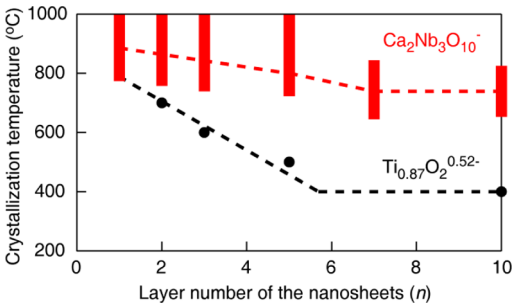

Figure 5. Layer number dependence of temperature for transformation into a mixture of $CaNb_2O_6$ and $Ca_2Nb_2O_7$. The red zone indicates the temperature range where the nanosheet structure transformed into $CaNb_2O_6$ and $Ca_2Nb_2O_7$. The data for the $Ti_{0.87}O_2^{0.52-}$ nanosheets are also included for comparison.[34]

We previously reported similar thermal stabilization of titania nanosheet ($Ti_{0.87}O_2^{0.52-}$) in their films with a thickness controlled by the number of nanosheet layers.[34] As plotted in Figure 5, the crystallization of anatase from the $Ti_{0.87}O_2^{0.52-}$ nanosheet was suppressed up to 800 °C in its monolayer form, which is much higher by 400 °C than the normal transformation temperature of the bulk samples. We discussed this behavior in terms of the scant quantity of a "reactant" to form a thermodynamically stable anatase structure. The titania nanosheet, being composed of only two edge-shared TiO_6 octahedra along the sheet normal, is very thin compared with the unit cell dimensions of the anatase structure. Thus, extensive migration and accumulation of Ti and O atoms *via* thermal activation are needed to promote the nucleation and subsequent growth of anatase crystallites. This situation is gradually relaxed in the thicker films, resulting in lower transformation temperatures. Indeed, the temperature decreased from 800 °C for the monolayer film to 400−500 °C for the five-layer one, which can be regarded as the bulk behavior.

The tendency observed in the $Ca_2Nb_3O_{10}^-$ nanosheet in the present study, the higher thermal stability of the thinner films, should be accounted for by this effect. For the thicker films, the saturated environment with excessive atoms should allow facile nucleation and rapid growth of thermodynamically stable phases at relatively low temperatures. Thus, bulk behavior appeared for the film thickness approaching ~10 nm. For the thinner films, however, nucleation and decomposition are severely hindered in the molecularly thin perovskite layers, and such a 2D bound reactant provides an unusual environment in structure reconstruction, causing the layer number dependence of the transformation temperature.

The structural features of $Ca_2Nb_3O_{10}^-$ nanosheets and $CaNb_2O_6$ are compared in Figure S7 (Supporting Information). The two structures are clearly different from each other, although they have some similarities. The packing of Ca, Nb, and O atoms per unit area are

comparable to each other when focused on the structure projections along the *c*- and *a*-axis, respectively. However, the atomic contents along the nanosheet normal are less than along the *a*-axis of $CaNb_2O_6$; one and two additional atomic planes of Ca and O, respectively, are needed to organize the unit cell of $CaNb_2O_6$ from a single layer of $Ca_2Nb_3O_{10}^-$. In this context, some moderate atomic migration/rearrangement may be still required for the transformation from a $Ca_2Nb_3O_{10}^-$ nanosheet into $CaNb_2O_6$ and $Ca_2Nb_2O_7$.

These results for $Ti_{0.87}O_2^{0.52-}$ and $Ca_2Nb_3O_{10}^-$ nanosheets should be understood as distinctive thermal behavior inherent to molecularly thin 2D systems. Note that this peculiar nature can be probed only with nanosheets, which can be precisely organized into high-quality multilayers. The thermal stabilization in $Ca_2Nb_3O_{10}^-$ nanosheets down to the monolayer from the bulk material is approximately 100 °C, which is much smaller than the case for $Ti_{0.87}O_2^{0.52-}$ nanosheets. This difference may be understood first by the high robustness of the perovskite-type system and second by its thicker nature as a reactant. The structural difference between $Ca_2Nb_3O_{10}^-$ nanosheets and $CaNb_2O_6/Ca_2Nb_2O_7$ is smaller than that for the titania system,[34] resulting in a rather weak dependence of the transformation temperature on the number of nanosheet layers.

Another interesting aspect observed in the crystallization of anatase from $Ti_{0.87}O_2^{0.52-}$ nanosheets is that the produced anatase nanocrystals grow preferentially along the *c*-axis when the nanosheet film is thin, *e.g.*, <3-layer film. This feature has been discussed in terms of the templating effect; the 2D nanosheet structure acts as a base for nucleation of the anatase lattice. In this study, the crystallized $CaNb_2O_6$ exhibited a strong 002 peak in the in-plane XRD data, while the 200 and 400 peaks were prominent in the out-of-plane data. The strongest peak for this phase in polycrystalline form is 311 (JCPDS No. 39-1392). These data indicate that $CaNb_2O_6$ produced in the film is oriented with the *a*-axis parallel to substrate normal, strongly suggesting the templating action of $Ca_2Nb_3O_{10}^-$ nanosheets. We observe some similarity in the in-plane ($b\times c$) atomic arrangement of $CaNb_2O_6$ and the 2D structure of the $Ca_2Nb_3O_{10}^-$ nanosheet (Supporting Information, Figure S7),[40] which may be responsible for facilitating such an effect.

Topographic Change. The unusual structure reconstruction discussed above can be monitored by AFM. Figure 6 presents the representative AFM images for the film samples in the temperature range where the structure change occurred. There was no noticeable change in 2D morphology, with an extremely flat surface for the monolayer film heated at 100−700 °C (Figure 6a). The initiation of crystallization at 800 °C is clearly observed by the formation of granular crystallites with heights of ~0.6−1.0 nm. Considering the XRD

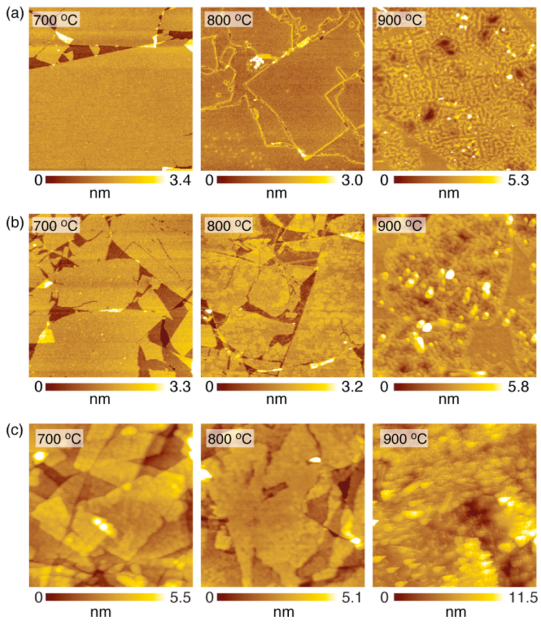

Figure 6. AFM images ($3 \times 3\ \mu m^2$) for (a) monolayer, (b) two-layer, and (c) five-layer films heated at 700, 800, and 900 °C.

data above, the evolved nanocrystals are attributable to $CaNb_2O_6/Ca_2Nb_2O_7$. Interestingly, these nanocrystals were formed in a line pattern, which suggests that the crumple or edge of the nanosheets provides an active site for the transformation. The abundance of the decomposed products, $CaNb_2O_6/Ca_2Nb_2O_7$, clearly increased at 900 °C, where the nanosheet boundaries became hardly distinguishable.

In the two-layer sample, the nanosheet appeared intact upon heating at 700 °C, while it became checkerwise at 800 °C, identified as a mixture of the unilamellar sheets and $CaNb_2O_6/Ca_2Nb_2O_7$ (Figure 6b). The segregated state at 800 °C presents a reasonable picture of ongoing transformation, and the domain size of $CaNb_2O_6/Ca_2Nb_2O_7$ nanocrystals increased at 900 °C as well. A topographic change similar to the case for the two-layer sample was observed in the three-layer sample (Figure S8a). In the five-layer sample, a granular texture was observed completely across the film at 800 °C (Figure 6c). Furthermore, the seven- and 10-layer film samples started to form $CaNb_2O_6/Ca_2Nb_2O_7$ nanocrystals at 700 °C (see Supporting Information, Figure S8b and S8c). These observations agree well with those revealed from XRD characterizations, indicating the facile crystallization of $CaNb_2O_6/Ca_2Nb_2O_7$ nanocrystals at a lower temperature for the thicker films.

We also note that these topological changes in Figure 6 are not artifacts induced by thermal damage in Si substrates. We employed AFM measurements of the bare Si substrates with the same thermal treatment. The AFM images revealed that there was no noticeable change in surface morphology and roughness even for annealing at 800 °C (Supporting Information, Figure S9). These results indicate that Figure 6 shows the intrinsic

properties of $Ca_2Nb_3O_{10}^-$ nanosheets free from substrate effects, providing a detailed understanding of the structural behavior of the nanosheets.

Films on Single-Crystal Substrate of $SrRuO_3$. Such a superior thermal stability is not specific to substrate selection and interface geometry. We fabricated 10-layer films on $SrRuO_3/SrTiO_3$, utilized as a bottom electrode for dielectric characterization. The out-of-plane XRD data revealed sharp basal peaks from well-stacked $Ca_2Nb_3O_{10}^-$ nanosheets along with those from the substrate (Figure 7), indicating the successful construction of the multilayer film. This feature was stable up to 700 °C except for the reduced peak intensity of the nanosheet film at 700 °C. Then, the feature completely changed at 800 °C into the one showing four peaks from $CaNb_2O_6$ as well as those from the substrate. This behavior is identical to that observed for the Si substrate.

AFM images revealed that the atomically flat morphology was maintained even after high-temperature annealing; the roughness was ~1.0 nm (Supporting Information, Figure S10). Cross-sectional high-resolution transmission electron microscopy (HRTEM) observations provided further information concerning the nanostructural change in the heating process (Figure 8). The well-ordered lamellar structure appeared intact for the film heated at 600 °C (Figure 8a), which is consistent with the XRD and AFM data described above. Ten layers of $Ca_2Nb_3O_{10}^-$ nanosheets assembled layer-by-layer were clearly observed. Each 1.5 nm thick nanosheet was further resolved into three equidistant dark contrast lines corresponding to the NbO_6 octahedral slabs in the nanosheet. These observed nanostructural features are similar to those in the as-deposited film without annealing, again proving the high thermal stability. More importantly, there was no detectable interdiffusion and strains at the interface, suggesting the persistence of the dead-layer-free feature up to 600 °C. Electron energy-loss spectroscopy (EELS) in TEM was used to probe compositional changes at the interface for the film heated at 600 °C (Figure 9). The Ca-L edge spectra showed a compositional abruptness between the $SrRuO_3$ substrate and subsequently deposited nanosheets; the lamellar parts (points 5−9) are composed of $Ca_2Nb_3O_{10}^-$. These results indicate that the high thermal stability of $Ca_2Nb_3O_{10}^-$ nanosheets possibly eliminates a low-*k* passive layer or any dead-layer effect at the interface; the interface reaction can be engineered out in the film heated below 600 °C.

For the film heated at 700 °C, however, we observed some regions where the multilayer structure started to degrade. For example, in a specified region as shown in Figure 8b, a smaller number of nanosheet layers, six or seven, was recognized, and the film surface exhibited rather featureless contrast, which may be identified as some amorphous or poorly crystalline materials. We also observed some regions where the multilayer structure

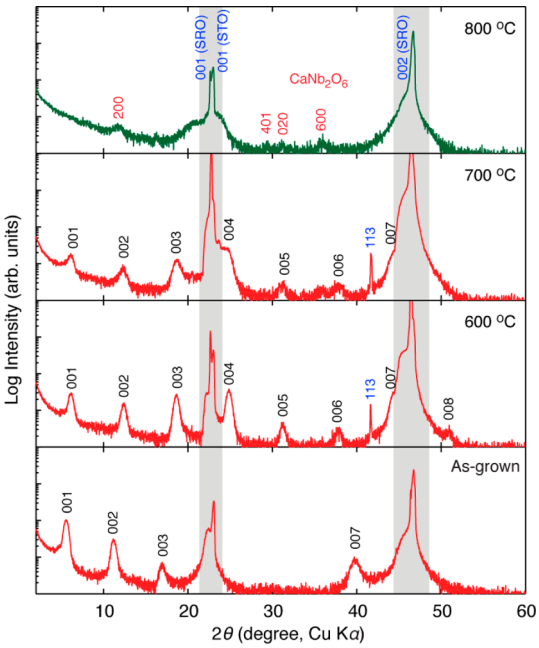

Figure 7. Out-of-plane XRD patterns for the 10-layer films on the $SrRuO_3/SrTiO_3$ single-crystal substrate. The peaks in the shaded zones are attributable to the substrate.

completely decomposed into amorphous or poorly crystalline materials (not shown here). However, the sample heated at 800 °C shows the formation of crystalline phases. The lattice image in Figure 8c is attributable to $CaNb_2O_6$. The *a*-axis is nearly perpendicular to the substrate, being compatible with the discussion above based on the XRD data. The phase transformation can also be monitored by selected-area electron diffraction (SAED) patterns. In the films heated at 600 and 700 °C (Figure 8d and e), in addition to the sharp spots from the $SrRuO_3/SrTiO_3$ single-crystal substrate, we also observed some weak spots arrayed in a line, which were assignable to 00*l* reflections from the stacked lamellar structure of the nanosheets. In the film heated at 800 °C, however, these weak spots disappeared and new diffraction spots indexable to the $CaNb_2O_6$ phase appeared. In addition, an interfacial dead layer was formed due to the large lattice mismatch between $CaNb_2O_6/Ca_2Nb_2O_7$ and the substrate. These results clearly indicate that nucleation and crystal growth are severely hindered in molecularly thin 2D perovskite-type nanosheets, and such a 2D bound reactant provides an unusual environment in structure reconstruction, resulting in robust thermal stability.

Effect of Thermal Stability on Dielectric Properties. We now turn to the effect of annealing on the dielectric properties of multilayer films. The leakage current and dielectric properties were investigated by preparing $Au/(Ca_2Nb_3O_{10}^-)_{10}/SrRuO_3$ capacitors. Such highly ordered films exhibited stable dielectric performance over a wide temperature range. Figure 10 presents the leakage current density *versus* voltage (*J*−*V*) curves for multilayer film $(Ca_2Nb_3O_{10}^-)_{10}$ heated at elevated temperatures. The films heated at 600 °C exhibited a

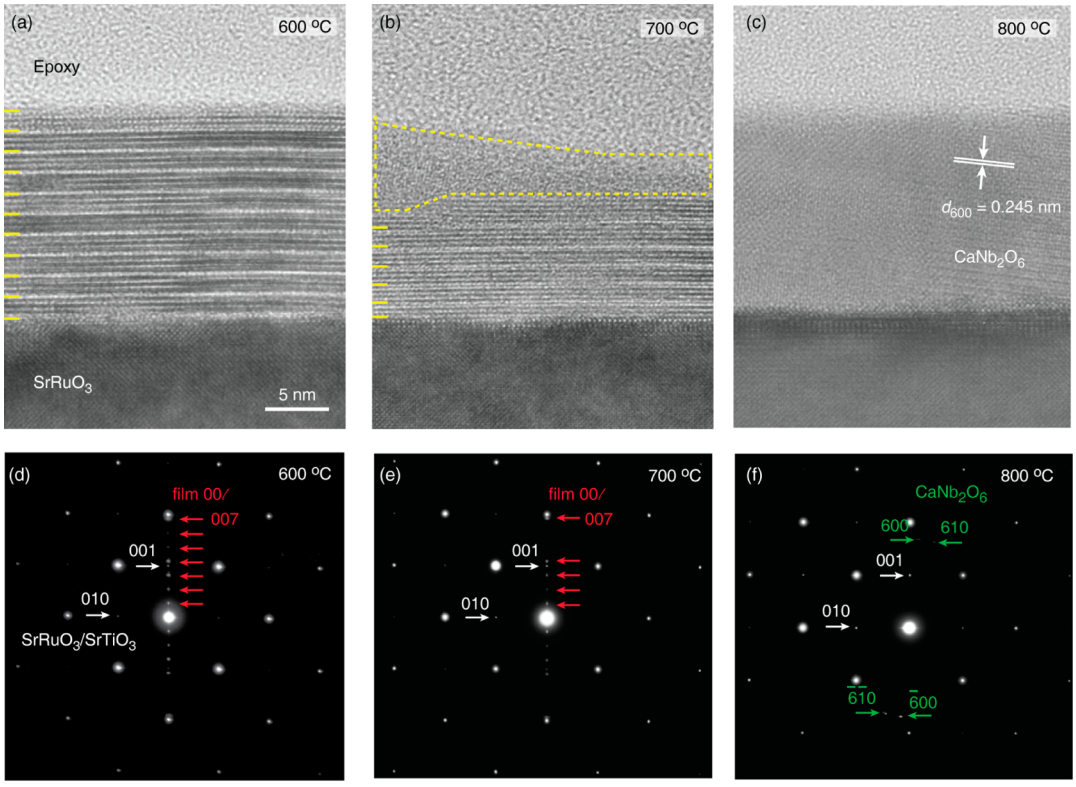

Figure 8. High-magnification HRTEM images of $(Ca_2Nb_3O_{10}^-)_{10}$ films on the $SrRuO_3$ substrate heated at (a) 600, (b) 700, and (c) 800 °C. The dashed outline in (b) denotes poorly crystallized or amorphous regions. Panels (d)−(f) show the corresponding SAED patterns.

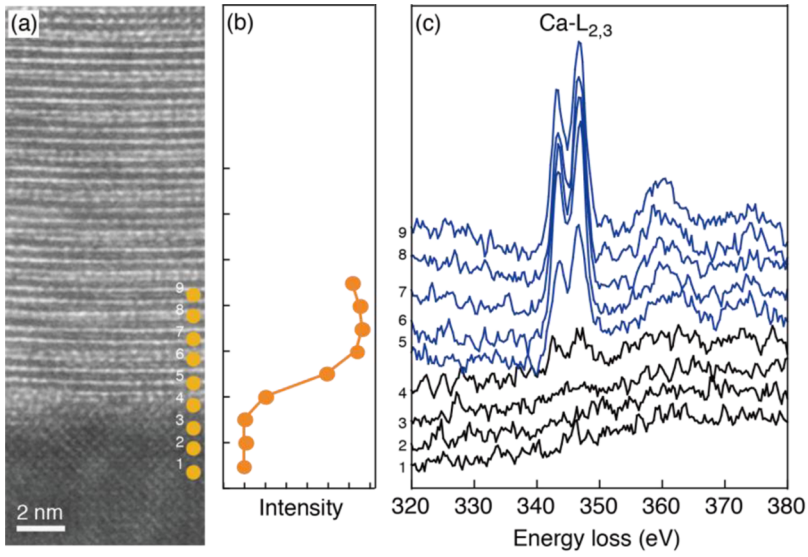

Figure 9. Interface characterization of a $(Ca_2Nb_3O_{10}^-)_{10}$ film on the $SrRuO_3$ substrate heated at 600 °C. (a) HRTEM image, (b) integrated intensity profile, and (c) spectra of the Ca-L edge EELS across the $(Ca_2Nb_3O_{10}^-)_{10}/SrRuO_3$ interface.

highly insulating nature similar to that observed in the as-deposited film without heating; the *J* value was on the order of 10^{-7} A cm^{-2} at +1 V. The insulating property is independent of the probe regions, indicating that the uniform films were stable at 600 °C. This situation was different in the films heated at 700 and 800 °C. The *J* curves strongly depended on the probe regions, which exhibited two different characteristics with low-resistance and high-resistance states (Figure 10b). In the low-resistance state, the *J* value was increased with applied voltage to reach $\sim 10^{-3}$ A cm^{-2} at +1 V. Considering the structural features, we assume that the low-resistance state is related to the $CaNb_2O_6/Ca_2Nb_2O_7$ nanodomains. The segregation of the $CaNb_2O_6/Ca_2Nb_2O_7$ nanodomains forms conducting paths, causing considerable leakage current.

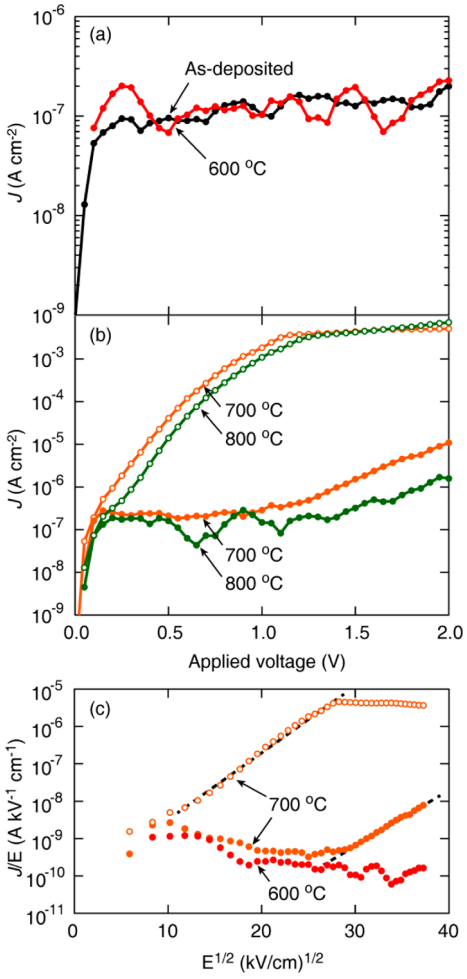

Figure 10. (a), (b) $J-V$, and (c) $J/E - E^{1/2}$ profiles of $Au/(Ca_2Nb_3O_{10}^-)_{10}/SrRuO_3$ annealed at elevated temperatures.

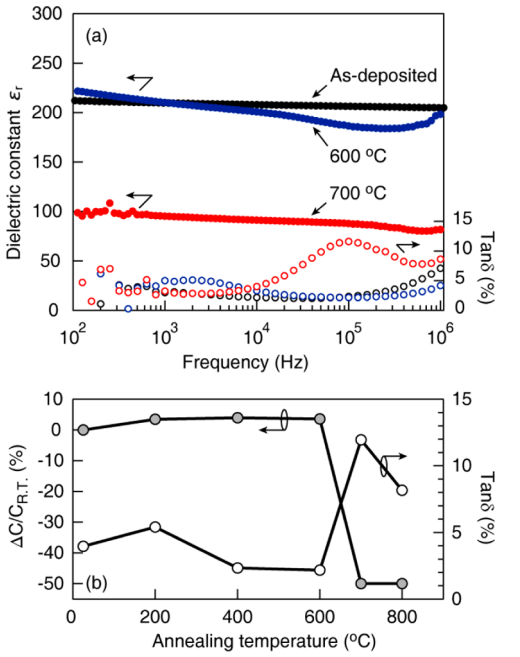

Figure 11. (a) Frequency dependence of ε_r and tan δ for $Au/(Ca_2Nb_3O_{10}^-)_{10}/SrRuO_3$ at selected temperatures. (b) Variation of capacitance and dielectric loss as a function of annealing temperature.

However, the high-resistance property arises from the multilayer structure of the persistent nanosheets. In $Au/(Ca_2Nb_3O_{10}^-)_n/SrRuO_3$ capacitors, the leakage current property is governed by a Schottky-type barrier, a contact between *n*-type nanosheet film and Au with a high work function that allows the electrons to flow from the film into the electrode. In the high-field region of >+1 V, the $J-V$ profiles of the film heated at 700 °C can be well fitted by the corresponding $\ln(J/E) - E^{1/2}$ plots (Figure 10c), suggesting that the conduction mechanism is governed by a Poole–Frenkel current. We also note that the film structures have a strong effect on the Schottky-type barrier. Indeed, the J values of the film heated at 800 °C were lower than those of the 700 °C case. This is likely due to improved crystallization as well as the increased amount of $CaNb_2O_6/Ca_2Nb_2O_7$ nanodomains. The $CaNb_2O_6/Ca_2Nb_2O_7$ has a larger band gap[41,42] than $Ca_2Nb_3O_{10}^-$ (3.4 eV),[43] yielding the suppression of the leakage current.

Figure 11a shows the frequency dependence of the relative dielectric constant (ε_r) and the dielectric loss (tan δ) for the film heated at elevated temperatures. The temperature variation is summarized in Figure 11b.

The dielectric responses reflect the film architecture in a similar manner to the leakage current properties. In the temperature range 25–200 °C, $Ca_2Nb_3O_{10}^-$ nanosheets exhibit a robust high-k response with a small variation of temperature; the temperature coefficient was τ = 100 ppm/K. The film heated at 600 °C still exhibited a high dielectric response (ε_r = 200) with a low tan δ (~5%), with the property being almost comparable to that observed in the as-deposited film.[32] For the film heated at 700 °C and above, the phase transformation caused a strong suppression of the dielectric response; the ε_r values were ~100, which was almost half of that observed in the as-deposited film. For the tan δ, Debye-like relaxation peaks were observed at ~100 kHz. These observations indicate that the different microstructural characteristics of nanocrystals cause a different dielectric response, particularly for lower frequencies. The film heated at 700 °C is composed of interfaces with the $CaNb_2O_6/Ca_2Nb_2O_7$ nanodomains in a large volume fraction. The polarization relaxation in the interfaces constructed by the $CaNb_2O_6/Ca_2Nb_2O_7$ nanodomains has a shorter relaxation time than that of the nanosheets stacked in multilayers. In this regard, the $CaNb_2O_6/Ca_2Nb_2O_7$ nanodomains may suppress dielectric responses.

Figure 12a shows the thickness dependence of the ε_r value for $Au/(Ca_2Nb_3O_{10}^-)_n/SrRuO_3$ (n = 3, 5, 10) at selected temperatures. For the films heated at 400 °C, the ε_r values remained constant at ~200 irrespective of the film thickness, a property that is almost comparable to the size-effect-free characteristic observed in the as-deposited film.[32] The films heated at 600 °C still exhibited

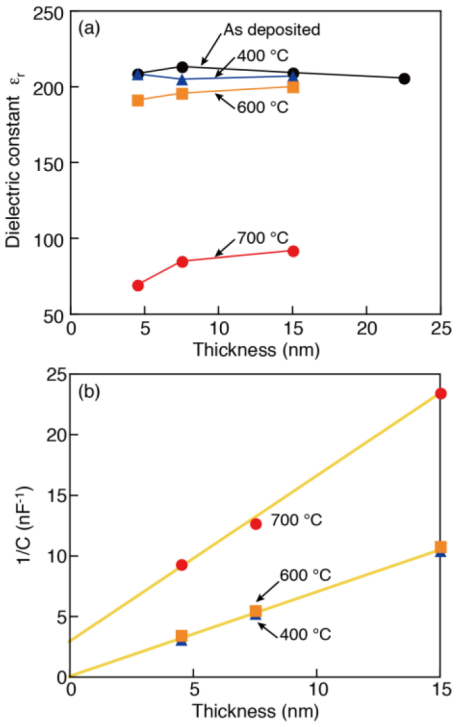

Figure 12. Thickness dependence of (a) the ε_r value and (b) the reciprocal capacitance 1/*C* for Au/$(Ca_2Nb_3O_{10}^-)_n$/$SrRuO_3$ (n = 3, 5, 10) at 400, 600, and 700 °C. In (a), the data for the as-deposited films are also included.[32]

high-*k* response (ε_r = 191−200) with a slight degradation at <10 nm. A size-induced degradation was clearly observed in the films heated at 700 °C. Figure 12b shows the thickness dependence of the reciprocal capacitance 1/*C* for the same films. In the 400 and 600 °C cases, the 1/*C* curves exhibited a linear relationship near the origin [a very small 1/*C* intercept (= 0.005−0.2 nF^{-1})], indicating a nearly negligible dead layer inside the films. In contrast, the 700 °C films possessed a large 1/*C* intercept due to the presence of a certain interfacial low-*k* dead layer ($1/C_{dead}$ = 2.9 nF^{-1}). Together with the interface characterization (Figure 9), we may conclude that the intrinsic dead layers can be engineered out in specific cases (heated at below 600 °C); the high thermal stability of $Ca_2Nb_3O_{10}^-$ nanosheets thus possibly eliminates the dead-layer effects at the interface.

These results offer new experimental inputs concerning the high-temperature use of perovskite-type nanosheets for electronic applications. Capacitors are ubiquitous in electronic devices and systems, and accordingly, the need for capacitors with stable electrical performance at elevated temperatures has increased in recent years. However, the lack of reliable high-temperature, high-*k* capacitors has almost certainly limited growth in these new applications. Conventional capacitor technologies, such as aluminum electrolytic or film capacitors, are limited to a maximum temperature range of ~150 °C or even lower. To achieve higher temperature ratings, ceramic and tantalum capacitors are employed. Some manufacturers have introduced products to satisfy the needs of the automotive industry, which have expanded the use of tantalum capacitors to engine compartment systems with operating temperatures of up to ~175 °C. The requirements for capacitor devices generally tend toward miniaturized dielectrics with higher permittivity, lower loss, and reduced leakage current. The present study of high-*k* perovskite-type nanosheets provides evidence of their potential technological impact as high-temperature capacitor materials. Indeed, perovskite-type nanosheets provide simultaneous improvements in the dielectric constant and dielectric strength properties of ultrathin forms of single-phase materials, which are also useful for application in high-temperature, high-energy-density capacitors. It is also crucial that applications for high-temperature electronics also ensure high reliability: the key requirements are maintaining optimum performance within specification and ensuring a long operating life. In this context, our preliminary experiments confirmed that the Au/$(Ca_2Nb_3O_{10}^-)_n$/$SrRuO_3$ nanocapacitor ensured a long operating life without obvious degradation of the ε_r and *J* properties (Supporting Information, Figure S11), further demonstrating the high reliability of nanosheet-capacitor technologies.

CONCLUSIONS

We have systematically investigated the thermal behavior of the perovskite-type $Ca_2Nb_3O_{10}^-$ nanosheet and its layer-by-layer assembled films. The monolayer film was stable up to 800 °C except for dehydration into "$Ca_2Nb_3O_{9.5}$", above which it started to segregate into a mixture of $CaNb_2O_6$ and $Ca_2Nb_2O_7$. The transformation temperature gradually decreased as the thickness of the nanosheet film increased and reached ~700 °C for seven- or 10-layered films. These results indicate that the $Ca_2Nb_3O_{10}^-$ nanosheet is thermally robust up to such high temperatures. In addition, the unique combination of a stable high-*k* dielectric response, low loss (<5%), and highly insulating nature ($J < 10^{-7}$ A cm^{-2}) persisted at least up to 600 °C.

These results clearly suggest that perovskite-type nanosheets are a model experimental system for future capacitor technology, and the solution-based layer-by-layer fabrication has great potential for the rational design and construction of nanoscale capacitor devices, compatible with current device fabrication lines with high-temperature processes. Manufactured components using perovskite-type nanosheets would exhibit constant fidelity over a wide range of frequency and temperature with low leakage current density, which is suitable for application in high-temperature, high-energy-density capacitors.

Such a thermally stable, ultrathin dielectric with superior high-*k* and insulating performance may also be used as a capacitor dielectric in Si-based

microelectronics. In the semiconductor industry, the need for nanometer-thick high-*k* dielectric films that exhibit good compatibility with Si is a crucial issue for future device development in dynamic random access memories (DRAMs) and metal-oxide-semiconductor field effect transistors (MOSFETs). Commercial DRAM and MOSFET devices require high-temperature thermal annealing (>500 °C) for fast and optimal device operation. Metal oxides such as Ta_2O_5, HfO_2, Ln_2O_3, and TiO_2 have been proposed as possible high-*k* gate insulators.[44,45] However, metal oxides with higher permittivity tend to have narrower band gaps, which leads to large leakage currents. In addition, most high-*k* oxides are thermodynamically unstable when placed in contact with Si and metal electrodes at an elevated temperature. Perovskite-type nanosheets exhibit good thermal stability (up to 600 °C) and larger band gap, which may respond to these demands.

METHODS

Materials Synthesis. The colloidal suspension of the perovskite-type nanosheet of $Ca_2Nb_3O_{10}^-$ was prepared by delaminating the layered perovskite compound of $KCa_2Nb_3O_{10}$ according to a previously described procedure.[27] The starting material, $KCa_2Nb_3O_{10}$, synthesized by a conventional solid-state reaction, was first converted into the acid-exchanged form of $HCa_2Nb_3O_{10}\cdot 1.5H_2O$ by repeated treatment with a 5 M HNO_3 solution. Next, the obtained protonic oxide was delaminated into colloidal nanosheets of $Ca_2Nb_3O_{10}^-$ *via* reaction with a TBA hydroxide solution. The resulting colloidal suspension contained unilamellar $Ca_2Nb_3O_{10}^-$ nanosheets with a lateral size of 2−5 μm, which was revealed by AFM observation.

The nanosheet films were prepared on various substrates such as glass, Si, and $SrRuO_3$ using the LB deposition process.[20,35,36,46−48] An atomically flat conducting $SrRuO_3$ substrate, consisting of a 50 nm thick (001)-oriented epitaxial $SrRuO_3$ film grown on a (001) $SrTiO_3$ single crystal, was used as a bottom substrate for dielectric property measurements. The $SrRuO_3$ substrate (1 × 1 cm^2) was photochemically cleaned using UV light irradiation in ozone, while the Si wafer and quartz glass substrates were cleaned by chemical treatment in a bath of 1:1 CH_3OH/HCl and then concentrated H_2SO_4 for 30 min each. A diluted colloidal suspension of the nanosheet (0.032 g dm^{-3}) was placed in the LB trough at a regulated temperature of 25 ± 0.5 °C. After 3 min, the surface of the suspension started to compress at a rate of 0.5 mm s^{-1} until the surface pressure reached 15 mN m^{-1}. After maintaining the constant pressure for 15 min, the nanosheets at the air/water interface were transferred onto the substrate through the vertical lifting of the substrate immersed in the LB trough at a transfer rate of 1.0 mm min^{-1}. Nearly full coverage of ∼95% with negligible overlaps between the nanosheets was attained at these optimized conditions. The LB transfer was repeated a specified number of times to fabricate a multilayer assembly composed of *n* layers (*n* = 1, 2, 3, 5, 7, and 10). The obtained film samples were irradiated by UV white light from a Xe lamp (4 mW cm^{-2}) for 24 h to completely decompose the TBA ions trapped in the nanosheet gallery. Heat treatment of these films grown on Si and $SrRuO_3$ substrates was performed by increasing the temperature from ambient temperature at a rate of 5 °C min^{-1} to a preset temperature (300, 400, 500, 600, 700, 800, 900, and 1000 °C). After keeping the samples at that temperature for 1 h, the samples were cooled naturally in the furnace.

Measurements and Analysis. UV−visible absorption spectra were recorded in a transmission mode using a Hitachi U-4100 spectrophotometer. Out-of-plane XRD data were collected by a Rigaku RINT 2200 powder diffractometer using monochromatized Cu Kα radiation (λ = 0.15405 nm). HRTEM images were acquired using a Hitachi H-9000 microscope operating at 200 kV. In-plane XRD analysis was performed with a four-axis diffractometer installed at the BL-6C in the Institute of Materials Structure Science, High Energy Accelerator Research Organization (KEK-PF). The incident X-ray was monochromated and focused on the incident slit (0.1 mm) by Si(111) double monochromators and a cylindrical Pt mirror fused on quartz. The resultant horizontal and vertical divergences were 0.15° and 0.30°, respectively. The incident angle to the sample surface was fixed below the critical angle of the total external reflection. The diffracted X-ray that passed through the Soller slit (0.45°) at the front side of the NaI scintillation counter was counted for 3 s at each sampling point (angular interval of 0.05°).

The topographical variation of the nanosheet films upon the heat treatment was monitored using an SII nanotechnology E-sweep AFM with a Si tip cantilever (14 N m^{-1}). Electrical measurement was performed by forming Au/$(Ca_2Nb_3O_{10}^-)_{10}$/$SrRuO_3$ capacitors. Au top electrodes (30 nm thick, 100 μm in diameter) were deposited using the vacuum evaporation method. The insulating and dielectric properties were characterized using a dielectric test system consisting of a semiconductor parameter analyzer (Keithley 4200-SCS) and a precision impedance analyzer (Agilent Technologies 4294A).

Conflict of Interest: The authors declare no competing financial interest.

Acknowledgment. This work was supported in part by the World Premier International Research Center Initiative on Materials Nanoarchitronics, MEXT, Japan. M.O. acknowledges support from the Industrial Technology Research Grant Program (06A22702d), NEDO, and the Grant-in-Aid for Scientific Research (25289232), MEXT, Japan.

Supporting Information Available: Additional figures. This material is available free of charge *via* the Internet at http://pubs.acs.org.

REFERENCES AND NOTES

1. Schlom, D. G.; Chen, L.-Q.; Pan, X. Q.; Schmehl, A.; Zurbuchen, M. A. A Thin Film Approach to Engineering Functionality into Oxides. *J. Am. Ceram. Soc.* **2008**, *91*, 2429–2454.
2. Dawber, M.; Rabe, K. M.; Scott, J. F. Physics of Thin-Film Ferroelectric Oxides. *Rev. Mod. Phys.* **2005**, *77*, 1083–1130.
3. Basceri, C.; Streiffer, S. K.; Kingon, A. I.; Waser, R. The Dielectric Response as a Function of Temperature and Film Thickness of Fiber-Textured (Ba,Sr)TiO_3 Thin Films Grown by Chemical Vapor Deposition. *J. Appl. Phys.* **1997**, *82*, 2497–2504.
4. Hwang, C. S. Thickness-Dependent Dielectric Constants of (Ba,Sr)TiO_3 Thin Films with Pt or Conducting Oxide Electrodes. *J. Appl. Phys.* **2002**, *92*, 432–437.
5. Kim, D. J.; Jo, J. Y.; Kim, Y. S.; Chang, Y. J.; Lee, J. S.; Yoon, J.-G.; Song, T. K.; Noh, T. W. Polarization Relaxation Induced by a Depolarization Field in Ultrathin Ferroelectric $BaTiO_3$ Capacitors. *Phys. Rev. Lett.* **2005**, *95*, 237602.
6. Parker, C. B.; Maria, J.-P.; Kingon, A. I. Temperature and Thickness Dependent Permittivity of (Ba,Sr)TiO_3 Thin Films. *Appl. Phys. Lett.* **2002**, *81*, 340–342.
7. Saad, M. M.; Baxter, P.; Bowman, R. M.; Gregg, J. M.; Morrison, F. D.; Scott, J. F. Intrinsic Dielectric Response in Ferroelectric Nano-Capacitors. *J. Phys.: Condens. Matter* **2004**, *16*, L451–L456.
8. Sinnamon, L. J.; Bowman, R. M.; Gregg, J. M. Investigation of Dead-Layer Thickness in $SrRuO_3$/$Ba_{0.5}Sr_{0.5}TiO_3$/Au Thin-Film Capacitors. *Appl. Phys. Lett.* **2001**, *78*, 1724–1726.
9. Streiffer, S. K.; Basceri, C.; Parker, C. B.; Lash, S. E.; Kingon, A. I. Ferroelectricity in Thin Films: The Dielectric Response of

Fiber-Textured $(Ba_xSr_{1-x})Ti_{1+y}O_{3+z}$ Thin Films Grown by Chemical Vapor Deposition. *J. Appl. Phys.* **1999**, *86*, 4565–4575.
10. Zhou, C.; Newns, D. M. Intrinsic Dead Layer Effect and the Performance of Ferroelectric Thin Film Capacitors. *J. Appl. Phys.* **1997**, *82*, 3081–3088.
11. Stengel, M.; Spaldin, N. A. Origin of the Dielectric Dead Layer in Nanoscale Capacitors. *Nature* **2006**, *443*, 679–682.
12. Fong, D. D.; Stephenson, G. B.; Streiffer, S. K.; Eastman, J. A.; Auciello, O.; Fuoss, P. H.; Thompson, C. Ferroelectricity in Ultrathin Perovskite Films. *Science* **2004**, *304*, 1650–1653.
13. Chu, Y. H.; Zhao, T.; Cruz, M. P.; Zhan, Q.; Yang, P. L.; Martin, L. W.; Huijben, M.; Yang, C. H.; Zavaliche, F.; Zheng, H.; *et al.* Ferroelectric Size Effects in Multiferroic $BiFeO_3$ Thin Films. *Appl. Phys. Lett.* **2007**, *90*, 252906.
14. Kim, Y. S.; Kim, D. H.; Kim, J. D.; Chang, Y. J.; Noh, T. W.; Kong, J. H.; Char, K.; Park, Y. D.; Bu, S. D.; Yoon, J. G.; *et al.* Critical Thickness of Ultrathin Ferroelectric $BaTiO_3$ Films. *Appl. Phys. Lett.* **2005**, *86*, 102907.
15. Garcia, V.; Fusil, S.; Bouzehouane, K.; Enouz-Vedrenne, S.; Mathur, N. D.; Barthélémy, A.; Bibes, M. Giant Tunnel Electroresistance for Non-Destructive Readout of Ferroelectric States. *Nature* **2009**, *460*, 81–84.
16. Ma, R.; Sasaki, T. Nanosheets of Oxides and Hydroxides: Ultimate 2D Charge-Bearing Functional Crystallites. *Adv. Mater.* **2010**, *22*, 5082–5104.
17. Sasaki, T. Fabrication of Nanostructured Functional Materials Using Exfoliated Nanosheets as a Building Block. *J. Ceram. Soc. Jpn.* **2007**, *115*, 9–16.
18. Osada, M.; Sasaki, T. Two-Dimensional Dielectric Nanosheets: Novel Nanoelectronics From Nanocrystal Building Blocks. *Adv. Mater.* **2012**, *24*, 210–228.
19. Sasaki, T.; Ebina, Y.; Tanaka, T.; Harada, M.; Watanabe, M.; Decher, G. Layer-by-Layer Assembly of Titania Nanosheet/Polycation Composite Films. *Chem. Mater.* **2001**, *13*, 4661–4667.
20. Li, B.-W.; Osada, M.; Akatsuka, K.; Ebina, Y.; Ozawa, T. C.; Sasaki, T. Solution-Based Fabrication of Perovskite Multilayers and Superlattices Using Nanosheet Process. *Jpn. J. Appl. Phys.* **2011**, *50*, 09NA10.
21. Sasaki, T.; Watanabe, M.; Hashizume, H.; Yamada, H.; Nakazawa, H. Macromolecule-like Aspects for a Colloidal Suspension of an Exfoliated Titanate. Pairwise Association of Nanosheets and Dynamic Reassembling Process Initiated from It. *J. Am. Chem. Soc.* **1996**, *118*, 8329–8335.
22. Tanaka, T.; Ebina, Y.; Takada, K.; Kurashima, K.; Sasaki, T. Oversized Titania Nanosheet Crystallites Derived from Flux-Grown Layered Titanate Single Crystals. *Chem. Mater.* **2003**, *15*, 3564–3568.
23. Omomo, Y.; Sasaki, T.; Wang, L. Z.; Watanabe, M. Redoxable Nanosheet Crystallites of MnO_2 Derived via Delamination of a Layered Manganese Oxide. *J. Am. Chem. Soc.* **2003**, *125*, 3568–3575.
24. Liu, Z.; Ma, R.; Ebina, Y.; Takada, K.; Sasaki, T. Synthesis and Delamination of Layered Manganese Oxide Nanobelts. *Chem. Mater.* **2007**, *19*, 6504–6512.
25. Schaak, R. E.; Mallouk, T. E. Perovskites by Design: A Toolbox of Solid-State Reactions. *Chem. Mater.* **2002**, *14*, 1455–1471.
26. Ozawa, T. C.; Fukuda, K.; Akatsuka, K.; Ebina, Y.; Sasaki, T. Preparation and Characterization of the Eu^{3+} Doped Perovskite Nanosheet Phosphor: $La_{0.90}Eu_{0.05}Nb_2O_7$. *Chem. Mater.* **2007**, *19*, 6575–6580.
27. Ebina, Y.; Sasaki, T.; Watanabe, M. Study on Exfoliation of Layered Perovskite-type Niobates. *Solid State Ionics* **2002**, *151*, 177–182.
28. Ebina, Y.; Akatsuka, K.; Fukuda, K.; Sasaki, T. Synthesis and In Situ X-ray Diffraction Characterization of Two-Dimensional Perovskite-Type Oxide Colloids with a Controlled Molecular Thickness. *Chem. Mater.* **2012**, *24*, 4201–4208.
29. Ozawa, T. C.; Fukuda, K.; Akatsuka, K.; Ebina, Y.; Sasaki, T.; Kurashima, K.; Kosuda, K. $Eu_{0.56}Ta_2O_7$: A New Nanosheet Phosphor with the High Intrananosheet Site Photoactivator Concentration. *J. Phys. Chem. C* **2008**, *112*, 1312–1315.
30. Ida, S.; Ogata, C.; Unal, U.; Izawa, K.; Inoue, T.; Altuntasoglu, O.; Matsumoto, Y. Preparation of a Blue Luminescent Nanosheet Derived from Layered Perovskite $Bi_2SrTa_2O_9$. *J. Am. Chem. Soc.* **2007**, *129*, 8956–8957.
31. Kim, J.-Y.; Chung, I.; Choy, J.-H.; Park, G.-S. Macromolecular Nanoplatelet of Aurivillius-Type Layered Perovskite Oxide, $Bi_4Ti_3O_{12}$. *Chem. Mater.* **2001**, *13*, 2759–2761.
32. Osada, M.; Akatsuka, K.; Ebina, Y.; Funakubo, H.; Ono, K.; Takada, K.; Sasaki, T. Robust High-*k* Response in Molecularly Thin Perovskite Nanosheets. *ACS Nano* **2010**, *4*, 5225–5232.
33. Wang, C.; Osada, M.; Ebina, Y.; Li, B.; Akatsuka, K.; Fukuda, K.; Sugimoto, W.; Ma, R.; Sasaki, T. All-Nanosheet Ultrathin Capacitors Assembled Layer-by-Layer *via* Solution-Based Processes. *ACS Nano* **2014**, *8*, 2658–2666.
34. Fukuda, K.; Ebina, Y.; Shibata, T.; Aizawa, T.; Nakai, I.; Sasaki, T. Unusual Crystallization Behaviors of Anatase Nanocrystallites from a Molecularly Thin Titania Nanosheet and Its Stacked Forms: Increase in Nucleation Temperature and Oriented Growth. *J. Am. Chem. Soc.* **2007**, *129*, 202–209.
35. Li, B.-W.; Osada, M.; Ozawa, T. C.; Ma, R.; Akatsuka, K.; Ebina, Y.; Funakubo, H.; Ueda, S.; Kobayashi, K.; Sasaki, T. Solution-Based Fabrication of Perovskite Nanosheet Films and Their Dielectric Properties. *Jpn. J. Appl. Phys.* **2009**, *48*, 09KA15.
36. Akatsuka, K.; Haga, M.; Ebina, Y.; Osada, M.; Fukuda, K.; Sasaki, T. Construction of Highly Ordered Lamellar Nanostructures through Langmuir-Blodgett Deposition of Molecularly Thin Titania Nanosheets Tens of Micrometers Wide and Their Excellent Dielectric Properties. *ACS Nano* **2009**, *3*, 1097–1106.
37. Fang, M.; Kim, C. H.; Mallouk, T. E. Dielectric Properties of the Lamellar Niobates and Titanoniobates $AM_2Nb_3O_{10}$ and $ATiNbO_5$ (A = H, K, M = Ca, Pb), and Their Condensation Products $Ca_4Nb_6O_{19}$ and $Ti_2Nb_2O_9$. *Chem. Mater.* **1999**, *11*, 1519–1525.
38. Cummings, J. P.; Simonsen, S. H. The Crystal Structure of Calcium Niobate ($CaNb_2O_6$). *Am. Mineral.* **1970**, *55*, 90–97.
39. Nanot, M.; Queyroux, F.; Gilles, J.-C.; Carpy, A.; Galy, J. Phases Multiples Dans Les Systèmes $Ca_2Nb_2O_7$-$NaNbO_3$ et $La_2Ti_2O_7$-$CaTiO_3$: Les Séries Homologues De Formule $A_nB_nO_{3n+2}$. *J. Solid State Chem.* **1974**, *11*, 272–284.
40. The atomic arrangement of $CaNb_2O_6$ enclosed by broken lines in Figure S7b has a close similarity to the 2D unit cell structure for a $Ca_2Nb_3O_{10}^-$ nanosheet (Figure S7a).
41. Cho, I.-S.; Kim, D. W.; Cho, C. M.; An, J. S.; Roh, H. S.; Hong, K. S. Synthesis, Characterization and Photocatalytic Properties of $CaNb_2O_6$ with Ellipsoid-like Plate Morphology. *Solid State Sci.* **2010**, *12*, 982–988.
42. Ikeda, S.; Fubuki, M.; Takahara, Y. K.; Matsumura, M. Photocatalytic Activity of Hydrothermally Synthesized Tantalate Pyrochlores for Overall Water Splitting. *Appl. Catal. A: Gen.* **2006**, *300*, 186–190.
43. Akatsuka, K.; Takanashi, G.; Ebina, Y.; Haga, M.; Sasaki, T. Electronic Band Structure of Exfoliated Titanium- and/or Niobium-Based Oxide Nanosheets Probed by Electrochemical and Photoelectrochemical Measurements. *J. Phys. Chem. C* **2012**, *116*, 12426–12433.
44. Kingon, A. I.; Maria, J.-P.; Streiffer, S. K. Alternative Dielectrics to Silicon Dioxide for Memory and Logic Devices. *Nature* **2000**, *406*, 1032–1038.
45. Wilk, G. D.; Wallace, R. M.; Anthony, J. M. High-*k* Gate Dielectrics: Current Status and Materials Properties Considerations. *J. Appl. Phys.* **2001**, *89*, 5243–5275.
46. Li, B.-W.; Osada, M.; Ozawa, T. C.; Akatsuka, K.; Ebina, Y.; Ma, R.; Ono, K.; Funakubo, H.; Sasaki, T. *A*-Site-Modified Perovskite Nanosheets and Their Integration into High-*k* Dielectric Thin Films with a Clean Interface. *Jpn. J. Appl. Phys.* **2010**, *49*, 09MA01.
47. Li, B.-W.; Osada, M.; Ozawa, T. C.; Ebina, Y.; Akatsuka, K.; Ma, R.; Funakubo, H.; Sasaki, T. Engineered Interfaces of Artificial Perovskite Oxide Superlattices *via* Nanosheet Deposition Process. *ACS Nano* **2010**, *4*, 6673–6680.
48. Osada, M.; Takanashi, G.; Li, B. W.; Akatsuka, K.; Ebina, Y.; Ono, K.; Funakubo, H.; Takada, K.; Sasaki, T. Controlled Polarizability of One-Nanometer-Thick Oxide Nanosheets for Tailored, High-*k* Nanodielectrics. *Adv. Funct. Mater.* **2011**, *21*, 3482–3487.